Journal of
Mechanics of
Materials and Structures

DIAGNOSIS OF CONCRETE DAMS BY FLAT-JACK TESTS AND
INVERSE ANALYSES BASED ON PROPER ORTHOGONAL DECOMPOSITION

Tomasz Garbowski, Giulio Maier and Giorgio Novati

■
■msp

DIAGNOSIS OF CONCRETE DAMS BY FLAT-JACK TESTS AND INVERSE ANALYSES BASED ON PROPER ORTHOGONAL DECOMPOSITION

TOMASZ GARBOWSKI, GIULIO MAIER AND GIORGIO NOVATI

Dedicated to the memory of Marie-Louise Steele and to Charles Steele.

Flat-jack tests have been employed for decades for the assessment of stresses and Young moduli in possibly deteriorated concrete dams and masonry structures. We propose a procedure for such tests that includes several innovations: identification of Young moduli and shear modulus in the presence of orthotropy, of pre-existing normal and shear stresses, and of tensile and compressive strength and fracture energy; use of full-field displacement measurements by digital image correlation (instead of extensometers); computer simulations performed once-and-for-all and productive of results which are subsequently processed out by proper orthogonal decomposition and its truncation; and identification of parameters in situ, soon after the tests, by portable computer with software able to perform inverse analyses by mathematical tools newly introduced into this context. The proposed procedure is validated by means of pseudoexperimental numerical exercises, by employing comparatively, as central computational tools, artificial neural networks and a trust region algorithm implying only first-order derivatives (with respect to the sought parameters) of the discrepancy function to minimize.

1. Introduction

Many concrete dams built up several decades ago in developed countries are at present deteriorated, with possible consequent decrease of safety margins with respect to limit states or collapses. A relatively frequent cause of damage in dam concrete is the physicochemical process called alkali-silica reaction: after a dormant period of several years from casting, a substantial decay of mechanical properties and an expansion generating self-stresses may occur slowly along a period of, say, thirty or forty years, with nonuniform distribution over the dam volume and sometimes without external visible manifestations of aging; see, for example, [Swamy 1992; Ahmed et al. 2003; Comi et al. 2009]. Such possible occurrences clearly require a rather large number of diagnostic analyses on a possibly damaged dam.

Structural diagnostic procedures of a mechanical nature employed in state-of-the-art dam engineering can be classified as follows (see [Maier et al. 2004], for instance): (a) quasi-nondestructive experiments by flat jacks on the dam surface [Fedele and Maier 2007]; (b) in depth coring or overcoring tests (similar to those which are traditional in geomechanics), usually with extraction of specimens for the laboratory (and, hence, destructive) [Goodman 1989; Fedele et al. 2005; Leite and Corthesy 2001]; (c) overall dynamical inverse analyses based on excitations by vibrodynes or by ambient vibrations and measurements by

accelerometers [Loh and Wu 2000]; (d) statical overall inverse analyses under loading due to ad hoc changes of water level in the reservoir, with measurements of consequent displacements by means of pendulums, collimators and/or interferometric radar [Fedele et al. 2006]; (e) same as (d), but with loading provided by seasonal, in-service variation of reservoir level (such alternative is much more economical than (d), however it requires more complex inverse analyses taking into account thermal effects as well [Ardito et al. 2008]).

Diagnostic procedures (c), (d) and (e) lead to the assessment of Young modulus only. Method (b) is clearly destructive and expensive. The limitations of procedure (a), traditionally applicable only to the estimation of the Young modulus and normal stresses, have been recently mitigated, so far only theoretically, in [Fedele et al. 2005] by recourse to test simulations and inverse analysis.

A step ahead in the development of structural diagnosis based on flat-jack tests and inverse analysis is provided in this paper, where the following novelties are presented and proposed to the engineering practice: (i) less destructive geometric configuration of the slots; (ii) use of digital image correlation (DIC) as full-field displacement measurement technique which economically provides much more experimental data than extensometers; (iii) assessment of inelastic parameters additional to elasticity and of the existing stress state (assumed as uniform, locally); (iv) parameter identification performed in a fast and inexpensive fashion (possibly in situ, using a portable computer) by a numerical procedure resting on proper orthogonal decomposition (POD), radial basis functions (RBF) interpolations and a trust region algorithm (TRA) or by an alternative procedure based on an artificial neural network (ANN).

Section 2 is primarily devoted to the operative sequence of the procedure to be carried out in situ, namely in selected locations on the dam surface. The computational procedures proposed for the estimation of elastic moduli and stresses are described, with some details and numerical validations, in the successive two sections: the techniques centered on POD–RBF–TRA in Section 3, and those based on POD–ANN in Section 4. In Section 5 preliminary research results are presented on the identification of plastic and fracture parameters. Section 6 is primarily devoted to prospects of further research.

2. Experimental procedure and its modeling

2.1. *Constitutive models.* Simple traditional constitutive models, still popular nowadays in dam engineering practice, have been adopted for the present investigation and validation exercises on the proposed parameter identification methods. Let the x-axis be horizontal on the dam free surface, assumed vertical for simplicity, let the z-axis be orthogonal to that surface, and, hence, axis y vertical as well. Anisotropy, specifically orthotropy with transversal isotropy in the horizontal plane, may be generated in dam concrete by the casting process, especially in roller compacted concrete, more and more frequently adopted in the last decade. In this case linear elasticity can be described as follows:

$$
\begin{pmatrix} \epsilon_x \\ \epsilon_y \\ \epsilon_z \\ \gamma_{xy} \\ \gamma_{yz} \\ \gamma_{xz} \end{pmatrix} = \begin{pmatrix} 1/E_H & -\nu_{VH}/E_V & -\nu_H/E_H & 0 & 0 & 0 \\ -\nu_{HV}/E_H & 1/E_V & -\nu_{HV}/E_H & 0 & 0 & 0 \\ -\nu_H/E_H & -\nu_{VH}/E_V & 1/E_H & 0 & 0 & 0 \\ 0 & 0 & 0 & 1/G_V & 0 & 0 \\ 0 & 0 & 0 & 0 & 1/G_V & 0 \\ 0 & 0 & 0 & 0 & 0 & 1/G_H \end{pmatrix} \begin{pmatrix} \sigma_x \\ \sigma_y \\ \sigma_z \\ \tau_{xy} \\ \tau_{xy} \\ \tau_{xz} \end{pmatrix}, \tag{1}
$$

$$\nu_{HV} = \nu_{VH}\frac{E_H}{E_V}, \qquad G_H = \frac{E_H}{2(1+\nu_H)}. \qquad (2)$$

The material parameters in (1) are the horizontal and vertical Young moduli, E_H and E_V; the in-plane (horizontal) and out-of-plane shear moduli, G_H and G_V; and the Poisson ratios ν_H, ν_{VH} and ν_{HV}, constrained by the relationships (2) due to the symmetry of the elastic compliance matrix and to the in-plane elastic energy balance (same as in the isotropic case), respectively. Therefore only five of these parameters are independent. The identification procedures developed in Section 3 and 4 will concern the three parameters E_H, E_V and G_V, which are the ones reasonably expected to play the main role in the system response in the hypothesis of transversal isotropy (in the horizontal plane) for the dam concrete. We assume a priori that $\nu_H = \nu_{VH} = 0.2$; the other parameters in (1) depend on the previous ones through (2).

Isotropy reduces to two the independent elastic parameters, say E and G (since $E_V = E_H = E$, $G_V = G_H = G$, $\nu_H = \nu_{HV} = \nu_{VH} = E/(2G) - 1$). The isotropy hypothesis will be used in Section 5 when focus is set on the identification of inelastic parameters.

The stress field pre-existing to the test and sought for by the identification procedure can be reasonably assumed to be a plane stress state ($\sigma_z = \tau_{zx} = \tau_{zy} = 0$), assumed as uniform over the whole volume affected by the test, hence governed by the three components $\sigma_H (= \sigma_x)$, $\sigma_V (= \sigma_y)$ and $\tau_{HV} (= \tau_{xy})$.

For the plastic behavior of concrete the classical Drucker–Prager model is adopted here (perfect plasticity with nonassociated flow rule), depicted in Figure 1a. Fracture is supposed to be first-mode only and reducible to a cohesive crack model with linear softening, as shown in Figure 1b in terms of normal stress σ versus opening displacement v. The assumptions above on the inelastic behavior of concrete lead to the following mathematical model formulation

$$F = t - p\tan\beta - d \le 0, \qquad d = \left(1 + \tfrac{1}{3}\tan\beta\right)f_t \qquad (3)$$

(see [Lubliner 1990; Jirasek and Bazant 2001], for instance). The meanings of the symbols in these formulas and in the figure are as follows: F is the yield function in the plane (Figure 1a) of the average normal stress p (compression positive) and of the equivalent shear t (I_1 being the first invariant of the stress tensor, J_2 the second invariant of the deviatoric stress tensor); the angles β and ψ represent internal friction and dilatancy of plastic flow, respectively; the cohesion d and the uniaxial strength f_t are related to each other by (3)$_2$, as a consequence of (3)$_1$. The dilatancy ψ is assumed to be $\psi = 40°$, a value frequently adopted in overall analyses of concrete dams in engineering practice. Thus the inelastic
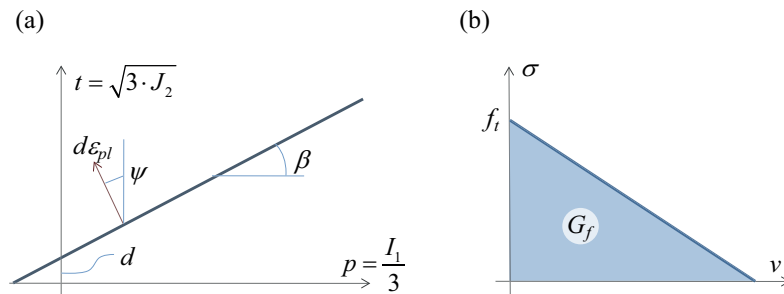
Figure 1. Material models and parameters relevant to diagnostic purposes: (a) Drucker–Prager no-hardening plasticity; (b) cohesive crack model with linear softening.
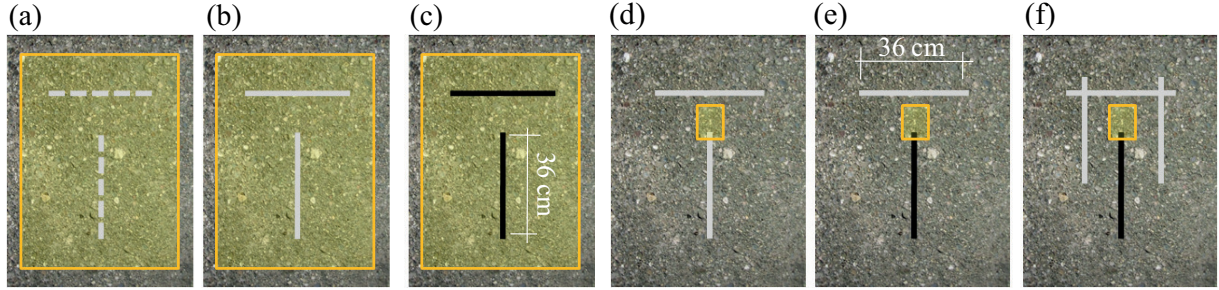
Figure 2. Sequence of steps in the parameter identification procedure: (a) positioning and (b) cutting of the slots (recording of displacements over the large ROI); (c) jacks inserted and pressurized (recording of displacements over the large ROI); (d) depressurization of jacks and change of ROI; (e) vertical jack pressurized to higher pressure level (displacements recorded over the smaller ROI).

parameters to estimate turn out to be three only: the internal friction β, the tensile strength f_t, and the fracture energy G_f. The uniaxial compressive strength f_c can be computed after model calibration through the following relationship, consequence of (3) for $F = 0$:

$$f_c = \frac{d}{1 - \frac{1}{3}\tan\beta} = \frac{\left(1 + \frac{1}{3}\tan\beta\right) f_t}{1 - \frac{1}{3}\tan\beta} . \tag{4}$$

2.2. *The test and its simulation.* The sequence of operative steps of the proposed diagnostic procedure based on flat-jack tests is outlined below with reference to Figure 2.

(a) In the selected place on the structure surface, the position of two future orthogonal slots (T-shaped geometry) is marked and a first photograph is taken by the DIC instrument over the region of interest (ROI) which is depicted in Figure 2a. In the DIC jargon (see [Hild and Roux 2006; Avril et al. 2008], for example), ROI is the area over which full-field measurements are performed; zone of interest (ZOI) is the image subset used by the image matching routine as a correlation window: comparing photos taken before and after the deformation, every ZOI of the initial image can be located in the deformed image through its "signature" in terms of gray-level values characterizing the pixel subset in point, as schematically illustrated in Figure 3. The displacement of the center point of a ZOI is computed as average of the displacements of the pixels inside the subset. A suitable grid is defined over the ROI, grid-nodes displacements being measurable by means of subsequent DIC photos.

(b) The two slots are cut (Figure 2b) and a second photo is shot by the DIC equipment so that, as mentioned, the displacements due to the release of the pre-existing stresses in the cut can be measured at all grid nodes and can be dealt with as accurately representative of the displacement full-field over the ROI.

(c) Two flat-jacks are inserted and pressurized by a piston-pumped liquid up to a pre-established pressure (Figure 2c). This pressure should correspond to a compromise between the needs to generate large enough, well measurable displacements in the ROI and to avoid nonnegligible inelastic strains. Again a DIC photo is taken over the ROI in order to capture the new displacement full-field.

(d) The horizontal jack is removed from its slot and the vertical one is depressurized. The original ROI employed in the preceding steps is replaced by a smaller ROI appropriate for focusing on one of the two
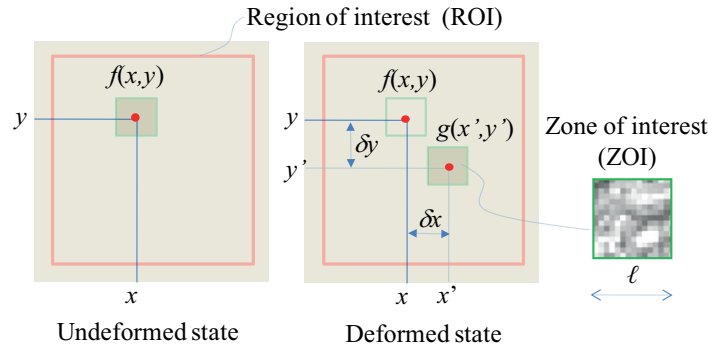
Figure 3. Schematic visualization of the DIC measurement procedure. The functions f and g are gray-level values; x, y are pixel coordinates in the ROI, and δx, δy are the displacement coordinates of the ZOI central point.

zones, located near the tips of the vertical slot, where inelastic deformations are expected (Figure 2d). A reference photo is taken of this ROI.

(e) The single flat-jack placed in the vertical slot is highly pressurized in order to generate plastic strains and a quasi-brittle fracturing process near the tips of the loaded slot where stress concentrations occur (Figure 2e). A sequence of DIC photos is taken to capture the nonlinear evolution of the displacements over the ROI, due to such pressure loading. The crack propagation is assumed as confined to the central vertical plane and to be stable, despite the softening in the cohesive crack behavior. Such localized fracture can be regarded as quasi-nondestructive in engineering terms. A possible provision to be adopted which can be beneficial in phase (e) for inelastic material characterization is the following one: two additional vertical slots (shown in Figure 2f) are cut in order to practically remove the influence on the fracture process of the horizontal stress; this, however, would make the test slightly more destructive. This variant is not investigated herein.

Based on these DIC measurements, the parameters identifications are performed according to the following sequence of phases (see caption of Figure 2): (I) elastic moduli, on the basis of experimental data concerning transition from stage (b) to (c); (II) stresses, on the basis of the elastic moduli estimates achieved in phase (I) and of data acquired at stages (a) and (b); (III) inelastic parameters, on the basis of data concerning the transition from stage (d) to the various deformation stages represented in the sequence of DIC photos taken in phase (e).

The finite element (FE) model here adopted for the subsequent computer simulations of the tests is depicted in Figure 4a as for the overall geometry and in Figure 4b as for the mesh. The FE discretization exhibits the following features: 97,600 tetrahedral elements with linear shape functions for displacements; 57,280 degrees of freedom; boundary conditions with vanishing displacements on the borders separating the domain from the surrounding volume supposed to be not perturbed by the test. It is worth noting that the ROI for DIC measurements is significantly reduced in moving from the identification of elastic moduli and stresses to the estimation of inelastic parameters: in fact for the latter inverse analyses concerning less uniform and more localized strains field, it is useful to exploit a higher density of the available DIC pixels.
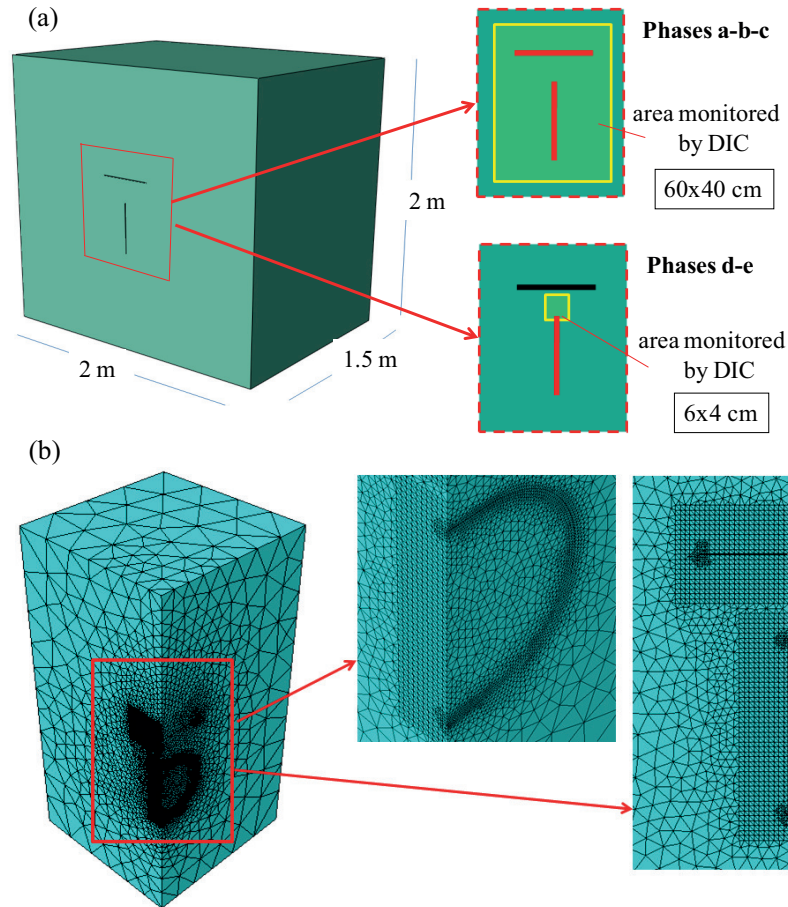
Figure 4. Finite element model for test simulations: (a) overall geometry and (b) mesh.

The simplicity of both the constitutive models and of the FE discretization for the numerical exercises presented in the two subsequent sections is motivated by the following circumstances: the present purpose is limited to a first numerical validation of novel procedures; consistency is pursued here with the assumptions and approximations at present adopted for real-life structural analyses of large concrete dams in view of inevitable uncertainties of several data.

A further simplification of test modeling concerns the flat-jacks: their configurations adopted at present would suggest to model the two steel laminae and the circumferential welds. Here uniform compressive traction is assumed throughout the concrete walls of the slot. Such assumption is reasonable: first, because it represents an acceptable approximation to the present purposes; second, because a new kind of flat jack based on textile laminae supported by a circumferential rod, now under investigation, is likely to be adopted in the future, thus making the assumption above more realistic.

For the numerical validation of the novel diagnostic procedures the adopted jack dimensions and test geometry are similar to those which are at present usual in traditional applications, consistent with usual sizes of aggregate in concrete. Clearly, larger dimensions with equal procedures can be adopted for dam concrete when the average aggregate size turns out to be larger.

3. Identification of elastic moduli and stresses by a POD–RBF–TRA procedure

3.1. *The inverse analysis procedure.* As usual in diagnostic inverse analyses, the domain in space over which the search for the material parameters can be confined should be preliminarily chosen according to expert judgment. For the present purposes, at first with reference to the estimation phase (I), the "feasible domain" is defined within the three-dimensional space of the elastic parameters in Table 1 by means of lower and upper bounds. Adopting the step values specified in this table, a grid with $M = 1089$ nodes is generated over the feasible domain.

For each of these sets of parameters the test simulation provides, by the FE model of Figure 4, the displacements measurable by DIC (over the ROI shown in Figure 2) relevant to the operative steps from (a) to (c), namely the displacements due to slot cutting and jack pressurization up to $p = 5$ MPa in the elastic range. The relative large size of the ROI makes immaterial, for identification by elastic modeling, the possible initial development of inelastic strains, localized near the slot tips, as the jack pressure approaches the maximum value ($p = 5$ MPa).

The DIC instruments here considered measure (and provide in digitalized form) $N = 2086$ displacement components (along horizontal and vertical axis on the dam surface, Figure 2a) at the nodes of the FE model (Figure 4) which coincide with the DIC grid nodes contained in the ROI (Figure 3).

The POD–RBF procedure. The clearly massive and heavy sequence of direct analyses based on the parameter vectors p_i ($i = 1, \ldots, M$) corresponding to grid nodes has been carried out by a commercial FE code (ABAQUS). Let the results be gathered in an $N \times M$ matrix U: its i-th column u_i is a vector, or *snapshot*, containing the N pseudoexperimental data belonging to the (now elastic) response to the pressure loading of the system with elastic moduli gathered in vector p_i.

Clearly, since the differences among the system responses arise only from variations of the sought parameters within the preselected domain in their space, the snapshots turn out to be correlated: they can be represented by "almost parallel" vectors in their space of $N = 2086$ dimensions. This correlation suggests the use of approximation, or *compression*, in the information contained in the snapshot matrix $U = [u_1 \cdots u_M]$ relevant to the elastic behavior of the system, by recourse to a proper orthogonal decomposition (POD) and truncation based on it.

The mathematical theory and computational procedures related to POD have origins remote in time and in application fields, and are now presented in a vast and still growing literature, of which we mention [Chatterjee 2000; Wu et al. 2003; Ostrowski et al. 2008]. Here only the specific procedure selected and applied to the present purposes is outlined, without analytical details.

Starting from the matrix U defined above, preliminarily obtained from M test simulations by FEM, the symmetric, positive semidefinite or definite matrix $D = U^T U$ is generated. Its (real, nonnegative)

	phase (I)			phase (II)					
	E_H/GPa	E_V/GPa	G_V/GPa	E_H/GPa	E_V/GPa	G_V/GPa	σ_H/MPa	σ_V/MPa	τ_{HV}/MPa
min	10	15	4	10	15	4	−6	−7	−2.5
step	1	1	1	5	5	4	1	1	0.5
max	20	25	12	20	25	12	−2	−1	−0.5

Table 1. Grid in parameter space for phases (I) and (II) of the identification procedure.

eigenvalues λ_i and the relevant normalized eigenvectors $\boldsymbol{v}_i$ are computed and employed to obtain the orthonormal basis

$$\boldsymbol{\Phi} = \left[\begin{array}{ccc} \boldsymbol{\Phi}_1 & \cdots & \boldsymbol{\Phi}_M \end{array}\right], \qquad \text{with} \qquad \boldsymbol{\Phi}_i = \boldsymbol{U}\boldsymbol{v}_i\lambda_i^{-1/2}. \tag{5}$$

In view of orthonormality, the $M \times M$ matrix $\boldsymbol{A}$ encoding the amplitudes $\boldsymbol{a}$ of the snapshots $\boldsymbol{u}$ is characterized by the relations

$$\boldsymbol{A} = \left[\begin{array}{ccc} \boldsymbol{a}_1 & \cdots & \boldsymbol{a}_M \end{array}\right] = \boldsymbol{\Phi}^T\boldsymbol{U}, \qquad \boldsymbol{U} = \boldsymbol{\Phi}\boldsymbol{A}. \tag{6}$$

The correlation among the snapshots (earlier noticed and reasonably expected for measurable responses to tests at varying parameters over the domain) make negligible many amplitudes $\boldsymbol{a}_i$ in the new basis $\boldsymbol{\Phi}$. It was mathematically proved (see e.g., [Nabney 2002; Liang et al. 2002]) that the eigenvalues λ_i quantify the negligibility of such amplitudes. By preserving only the $\overline{M}$ largest eigenvalues, with $\overline{M} \ll M$, an approximation $\overline{\boldsymbol{U}}$ is achieved of the $N \times M$ snapshot matrix $\boldsymbol{U}$ by means of a truncated basis $\overline{\boldsymbol{\Phi}}$ ($N \times \overline{M}$) and the relevant truncated $\overline{M} \times M$ amplitudes $\overline{\boldsymbol{A}}$, namely

$$\overline{\boldsymbol{U}} = \overline{\boldsymbol{\Phi}}\,\overline{\boldsymbol{A}} \cong \boldsymbol{U}, \qquad \text{whence} \qquad \overline{\boldsymbol{A}} = \overline{\boldsymbol{\Phi}}^T\boldsymbol{U}. \tag{7}$$

The approximation in $(7)_1$ is regarded as acceptable and negligible in subsequent developments, so that the amplitudes in $\overline{\boldsymbol{A}}$ are henceforth computed by $(7)_2$.

These developments often turn out to be computationally heavy but need to be done once-and-for-all as preparatory work generating matrices $\overline{\boldsymbol{\Phi}}$ and $\overline{\boldsymbol{A}}$: these condense ("compress") the information on the system behavior contained in the much larger matrix $\boldsymbol{U}$ and can be accommodated in a small computer to be employed "in situ".

The snapshot $\boldsymbol{u}$ corresponding to any "new" parameter vector $\boldsymbol{p}$ (new because not included as node in the preselected grid over the feasible domain in the parameter space) now can be assessed through (7) by means of its "amplitude" $\overline{M}$-vector $\bar{\boldsymbol{a}}(\boldsymbol{p})$. This amplitude can be expressed by means of radial basis function (RBF) interpolation (see, e.g., [Wu 1995; Buhmann 2003; Hassing et al. 2010]) using the known amplitude vectors $\bar{\boldsymbol{a}}_i(\boldsymbol{p}_i)$ corresponding to grid-nodes vectors $\boldsymbol{p}_i$, $i = 1, \ldots, M$:

$$\bar{a}_k(\boldsymbol{p}) = \sum_{i=1}^M b_i^k \, g(\boldsymbol{p}, \boldsymbol{p}_i) = \boldsymbol{g}^T(\boldsymbol{p})\boldsymbol{b}^k \qquad k = 1, \ldots, \overline{M}, \tag{8}$$

where $\bar{a}_k(\boldsymbol{p})$ is the k-th component of $\bar{\boldsymbol{a}}(\boldsymbol{p})$, the b_i^k are the interpolation coefficients and $g(\boldsymbol{p}, \boldsymbol{p}_i)$ are the radial functions; the vectors $\boldsymbol{g}^T(\boldsymbol{p})$ and $\boldsymbol{b}^k$ gather functions and coefficients, respectively. The cubic RBFs

$$g(\boldsymbol{p}, \boldsymbol{p}^i) = \|\boldsymbol{p} - \boldsymbol{p}_i\|^3 \tag{9}$$

where $\| \cdot \|$ is the Euclidean norm, are adopted here for the interpolation above. For each component k, Equation (8), enforced at the j-th node ($j = 1, \ldots, M$) of the parameter grid, takes the form $[\bar{\boldsymbol{a}}_j(\boldsymbol{p}_j)]_k = \boldsymbol{g}^T(\boldsymbol{p}_j)\boldsymbol{b}^k$. Assembling all M equations of this type, the following linear system is obtained, with the coefficients b_i^k as unknowns:

$$\boldsymbol{G}\boldsymbol{b}^k = [\,k\text{-th row of matrix } \bar{\boldsymbol{A}}\,]^T, \qquad k = 1, \ldots, \overline{M}, \tag{10}$$

where $\boldsymbol{G} = (G_{ji})$ with $G_{ji} = g(\boldsymbol{p}_j, \boldsymbol{p}_i)$. All the $\overline{M}$ linear equation systems to be solved share the same coefficient matrix (which is independent of k).

When matrix $\boldsymbol{B} = [\boldsymbol{b}^1 \ldots \boldsymbol{b}^k \ldots \boldsymbol{b}^{\overline{M}}]$ is available, the interpolation, (8), provides the truncated amplitude vector $\bar{\boldsymbol{a}}$ corresponding to any new parameter vector $\boldsymbol{p}$: $\bar{a}_k(\boldsymbol{p}) = [\boldsymbol{g}(\boldsymbol{p})]^T \boldsymbol{b}^k$; and, hence, (7) leads to the snapshot $\boldsymbol{u}$ of the N measurable quantities, namely to an approximation consistent with the preceding POD process. Formally:

$$\boldsymbol{u}(\boldsymbol{p}) \cong \overline{\boldsymbol{\Phi}} \; \bar{\boldsymbol{a}}(\boldsymbol{p}) = \overline{\boldsymbol{\Phi}} \; \boldsymbol{B}^T \boldsymbol{g}(\boldsymbol{p}) \tag{11}$$

where the $M-$vector $\boldsymbol{g}$ contains the values of the considered RBFs at the parameter node $\boldsymbol{p}$.

Clearly, (11) may replace with substantial savings test simulations (direct analyses) by FE computer codes or by other computing tools. This circumstance becomes very meaningful and practically advantageous in inverse analysis of the present kind.

In the present context parameter identification means minimization of a traditional discrepancy function ω of the residuals $\boldsymbol{R}$ (differences between experimental data $\boldsymbol{u}_s$ and their computed counterparts $\boldsymbol{u}_c$). Traditionally, the function ω is formulated as quadratic form with the inverse of the covariance matrix $\boldsymbol{C}$ of the experimental measures:

$$\min_{\boldsymbol{p}} \; \omega(\boldsymbol{p}) = \min_{\boldsymbol{p}} \left\{ \boldsymbol{R}^T(\boldsymbol{p}) \, \boldsymbol{C}^{-1} \boldsymbol{R}(\boldsymbol{p}) \right\} \tag{12}$$

where

$$\boldsymbol{R}(\boldsymbol{p}) = \boldsymbol{u}_s - \boldsymbol{u}_c(\boldsymbol{p}). \tag{13}$$

In view of the "pseudoexperimental" approach of the present investigation, it is assumed herein $\boldsymbol{C} = \boldsymbol{I}$ (identity matrix) without methodological limitations.

In order to numerically solve the problem formulated by (12), the popular trust region algorithm (TRA) is employed in this section and it is outlined below (for details see e.g., [Coleman and Li 1996; Conn et al. 2000]).

The Jacobian $\boldsymbol{J}$, the gradient $\partial \omega / \partial \boldsymbol{p}$ of the objective function ω and an approximation of the Hessian $\boldsymbol{H}$ read, respectively:

$$\boldsymbol{J}(\boldsymbol{p}) = \frac{\partial \boldsymbol{R}}{\partial \boldsymbol{p}}, \qquad \frac{\partial \omega}{\partial \boldsymbol{p}} = \boldsymbol{J}^T \boldsymbol{R}, \qquad \boldsymbol{H}(\boldsymbol{p}) = \frac{\partial^2 \omega}{\partial \boldsymbol{p}^T \partial \boldsymbol{p}} \simeq \boldsymbol{J}^T \boldsymbol{J}. \tag{14}$$

In each iteration, say the j-th one starting from the current point $\boldsymbol{p}_j$, the following two-variable mathematical programming problem has to be solved:

$$\min_{\alpha, \beta} \left\{ \tfrac{1}{2} \boldsymbol{s}_j^T \boldsymbol{J}^T \boldsymbol{J} \boldsymbol{s}_j + \left(\frac{\partial \omega}{\partial \boldsymbol{p}} \right)^T \boldsymbol{s}_j, \quad \|\boldsymbol{s}_j\| \leq \Delta_j \right\}, \tag{15}$$

where

$$\boldsymbol{s}_j = \alpha \boldsymbol{J}_j^T \boldsymbol{R}_j - \beta (\boldsymbol{J}_j^T \boldsymbol{J}_j)^{-1} \frac{\partial \omega}{\partial \boldsymbol{p}}. \tag{16}$$

In (15) Δ_j defines the "trust region" to be possibly adjusted after check according to criteria specified e.g., in [Nocedal and Wright 1999; Conn et al. 2000].

The iteration j of the first-order TRA described by (15) and (16) requires a multiplicity of first derivatives specified in (14) and numerically approximated here by forward finite differences. Therefore a high number of direct analyses are necessary in each application of TRA to the present inverse problem.

As for TRA and similar sequential mathematical programming technique, the computational burden is increased by possible nonconvexity (namely by possible local minima) of the objective function

$\omega(\boldsymbol{p})$ which may require different initializations (even if once-and-for-all for a specific kind of technical situations). In parameter identification problems where lack of discrepancy function convexity is expected, genetic algorithms may be an advantageous alternative (not examined herein) to mathematical programming, and the preliminary POD–RBF procedure above becomes very desirable for practical applications in view of the high number of required direct analyses. Computational savings may arise from POD–RBF also for sensitivity analysis of many measurable quantities (see [Kleiber et al. 1997], for example); however, we will not consider this topic further.

In the present diagnostic method the inevitably sequential estimation of parameters (elastic-stresses-inelastic, Section 2, Figure 2) implies an increase of the parameter space dimensionality and hence a growth (exponential at equal density) of the number M of grid nodes (and snapshots).

The advantages achievable by the procedure POD–RBF–TRA proposed herein in association with DIC and flat-jack tests for the identification, in sequence, of elastic moduli and stresses, are evidenced by numerical examples in Section 3.2.

In the POD–RBF procedure just outlined, truncation represents a clearly important step. The choice of number $\overline{M}$ of the preserved eigenvalues of matrix $\boldsymbol{D}$ (much below the number M of snapshots) can be decided by various criteria (besides the one based on eigenvalues λ_i, here without a direct physical meaning), two of which are particularly suitable to the present context: (i) meaningful difference between a snapshot resulting from a test simulation by FE analysis and the corresponding snapshot computed by POD–RBF with truncations; (ii) assessment of intrinsic accuracy of POD–RBF at varying the dimensionality $\overline{M}$ of the new basis $\overline{\boldsymbol{\Phi}}$. The latter has been adopted in the present study and is outlined in what follows.

Outside the nodes grid but still within the preselected domain, $\hat{M}$ parameter vectors $\hat{\boldsymbol{p}}_j$ are randomly generated (here $\hat{M} = 100$), and corresponding snapshots of pseudoexperimental data are computed through FE simulations of the same test. Random noise (here $\pm 5\,\mu\mathrm{m}$) is added to each snapshot which thus becomes $\hat{\boldsymbol{u}}_j$ ($j = 1, \ldots, \hat{M}$). The amplitude vector corresponding to $\hat{\boldsymbol{u}}_j$ is computed using (7):

$$\bar{\boldsymbol{a}}_j(\hat{\boldsymbol{p}}_j) = \overline{\boldsymbol{\Phi}}^T \hat{\boldsymbol{u}}_j(\hat{\boldsymbol{p}}_j), \qquad j = 1, \ldots, \hat{M}. \tag{17}$$

Now an approximation to such amplitude vector has to be attainable by RBF interpolation through (8) (employing the matrix $\boldsymbol{B}$) in correspondence with some $\boldsymbol{p}$:

$$\bar{\boldsymbol{a}}^{\mathrm{RBF}}(\boldsymbol{p}) = \boldsymbol{B}\,\boldsymbol{g}(\boldsymbol{p}). \tag{18}$$

Such $\boldsymbol{p}$ can be singled out by defining (for each j-th off-grid node) a residual

$$\boldsymbol{R}_j(\boldsymbol{p}) = \bar{\boldsymbol{a}}_j(\hat{\boldsymbol{p}}_j) - \bar{\boldsymbol{a}}^{\mathrm{RBF}}(\boldsymbol{p}) \tag{19}$$

and then by solving the problem

$$\boldsymbol{p}_j^* = \text{value of } \boldsymbol{p} \text{ that minimizes } \boldsymbol{R}_j^T(\boldsymbol{p})\,\boldsymbol{R}_j(\boldsymbol{p}). \tag{20}$$

The j-th parameter vector $\hat{\boldsymbol{p}}_j$ originally considered is now compared to its counterpart $\boldsymbol{p}_j^*$ resulting from minimization (20). Their difference can be regarded as representative of the RBF approximation in this j-th numerical test. An overall quantification of such error for the whole set of $\hat{M}$ off-grid nodes, i.e.,
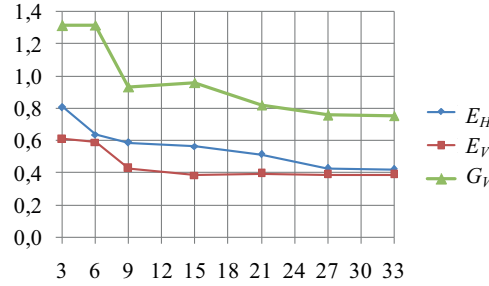
Figure 5. Errors, according to (21), in the elastic moduli due to the POD–RBF preliminaries as a function of the adopted truncation index $\bar{M}$.

the mean error according to (21) below, can be regarded as an assessment of the approximation induced by the POD–RBF scheme:

$$(\text{mean error})_l = \frac{1}{\hat{M}} \sum_{j=1}^{\hat{M}} \left| \frac{(\hat{\boldsymbol{p}}_j)_l - (\boldsymbol{p}_j^*)_l}{(\hat{\boldsymbol{p}}_j)_l} \right| \tag{21}$$

where subscript l denotes the l-th component of the parameters vectors. Figure 5 shows the mean error resulting for the elastic constants as a function of POD truncation index $\bar{M}$.

3.2. *Validation by computational examples.* This subsection gathers a sequence of selected numerical checks of potentialities and limitations of the (deterministic, least squares) diagnostic method presented in what precedes.

(A) First, inverse analyses have been carried out comparatively by TRA only, with the following provisions: (i) various initializations in order to check the well-posedness of the problem and, particularly, absence of local minima; (ii) random perturbations of the (pseudo) experimental input data in order to check their consequences on the estimates; (iii) same estimation procedure applied comparatively on the basis of DIC data and on the basis of extensometric data which are traditionally acquired with standard flat-jack tests.

The reference values of the parameters used in identification examples, carried out by TRA only, concerning phase (I) and phase (II), are as follows:

elastic parameters: $E_{\mathrm{H}} = 15\,\mathrm{GPa}$ $E_{\mathrm{V}} = 20\,\mathrm{GPa}$ $G_{\mathrm{V}} = 8\,\mathrm{GPa}$ $\nu_{\mathrm{H}} = \nu_{\mathrm{VH}} = 0.2$

pre-existing stresses: $\sigma_{\mathrm{H}} = -3\,\mathrm{MPa}$ $\sigma_{\mathrm{V}} = -5\,\mathrm{MPa}$ $\tau_{\mathrm{HV}} = -1\,\mathrm{MPa}$

All three kinds of evaluations led to positive and encouraging results starting from these reference values, with pseudomeasurements by DIC and by the FE model (Figure 4) same as those specified in Section 2; pressure of 5 MPa in both jacks; random noises on input data over intervals of $\pm 2.5\,\mu\mathrm{m}$ and then of $\pm 5.0\,\mu\mathrm{m}$, with uniform probability distribution.

Figure 6 indicates satisfactory stability of the TRA identification with respect to realistic random errors of DIC pseudoexperimental data considered. For comparison purposes, Figure 7a shows possible measurements by extensometers (specifically, linear variable differential transducers) employed at present in dam engineering. The elongation of $8+8$ segments between marks are intended to be monitored

(a)   (b)
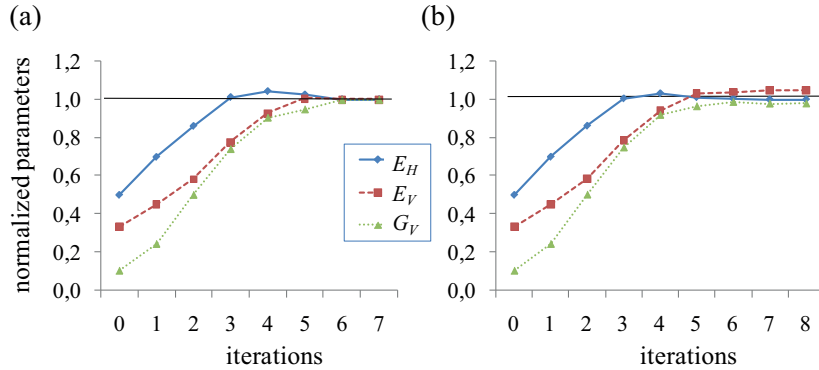
Figure 6. Identification of elastic parameters by TRA with different random perturbations of input data: (a) $\pm 2.5 \,\mu$m; (b) $\pm 5.0 \,\mu$m.

(a)   (b)
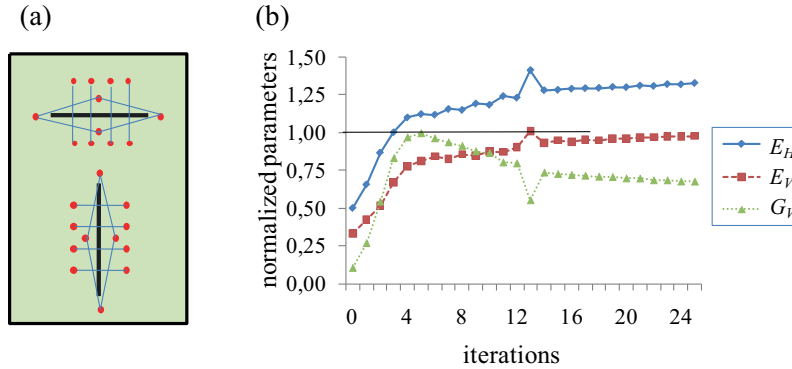
Figure 7. (a) Extensometric measurements and (b) consequent identification of elastic parameters (normalized by the reference values) by TRA inverse analysis.

and affected by $\pm 5.0 \,\mu$m random errors. Actually the considered noise and measurement number are rather optimistic when compared to the current practice based on extensometers. A TRA inverse analysis similar to the one leading to Figure 6 has been performed, but now on the basis of snapshots consisting of the 16 extensometric measurements shown in Figure 7a. Lack of convergence turns out to occur with extensometers in the comparative example illustrated by Figures 6b and 7b.

(B) The potentiality and accuracy of the whole procedure POD–RBF–TRA have been tested by numerical exercises like those summarized here below.

With reference to phase (I) of the identification procedure, Table 1 specifies the uniform grid chosen over the three-dimensional domain of the elastic parameters: the number of nodes amounts to $M = 1089$. Using this grid, the snapshots $\boldsymbol{u}$ (over the ROI) are computed by FE simulation as response to jack pressurization at 5 MPa of the two slots, and the corresponding matrices $\bar{\boldsymbol{\Phi}}$ and $\boldsymbol{B}$ are generated according to the POD–RBF procedure described in Section 3 (see page 187). Here the truncation adopted is quantified by $\bar{M} = 3$. On this basis, for any parameter vector $\boldsymbol{p}$ in the feasible domain, the corresponding snapshot $\boldsymbol{u}$ can be obtained in a fast way by (11) once the vector $\boldsymbol{g}(\boldsymbol{p})$ is computed.

Subsequently a set of $\hat{M} = 100$ off-grid parameter vectors $\hat{\boldsymbol{p}}_j$ is randomly generated and the corresponding snapshots $\hat{\boldsymbol{u}}_j$ (over the ROI) are computed through FE simulations analogous to the previous ones. Such snapshots, after perturbation by random noise addition, are used as pseudoexperimental data relevant to the transition from step (b) to step (c) of the test, Figure 2. For each $\hat{\boldsymbol{p}}_j$, the minimization (12) is carried out, with $\hat{\boldsymbol{u}}_j$ (now noised) playing the role of $\boldsymbol{u}_s$, vector $\boldsymbol{u}_c(\boldsymbol{p})$ being expressible via (11) on the basis of the chosen grid. Here the adopted noise value is $\pm 5 \,\mu$m.

The j-th parameter vector $\hat{\boldsymbol{p}}_j$ originally considered is now compared to its counterpart $\boldsymbol{p}_j^{**}$ identified through the minimization (12) and the accuracy of the estimation of each elastic parameter is assessed. For the j-th identification, the error of the computed estimate $(\boldsymbol{p}_j^{**})_l$ takes the form

$$\text{(error)}_{jl} = \left| \frac{(\hat{\boldsymbol{p}}_j)_l - (\boldsymbol{p}_j^{**})_l}{(\hat{\boldsymbol{p}}_j)_l} \right|, \qquad j = 1, \dots, 100, \qquad l = 1, \dots, 3. \tag{22}$$

Figure 8a shows the results obtained for the three elastic moduli by means of the 100 inverse analyses discussed above. In each histogram, the abscissa gives a range for the error of the estimate (in percent), and the ordinate gives the percentage of cases in which the error lies in the corresponding interval. The mean error, for the set of $\hat{M}$ identifications, amounts to 1.02%, 0.99% and 1.87% for the moduli E_{H}, E_{V} and G_{V}, respectively.

We next discuss phase (II) of the diagnostic procedure, the estimation of the pre-existing stresses. The preliminary POD–RBF procedure must concern not only the three stress components, but also the three elastic moduli. The six-dimensional grid is specified in Table 1 and has $M = 3375$ nodes. To avoid too high a value of M and consequent high computational burden for the preliminary POD–RBF, the steps adopted for E_{H}, E_{V} and G_{V} in phase (II) are much larger than those in phase (I), as shown in the table. As for the truncation leading to the new basis $\overline{\boldsymbol{\Phi}}$, (7), the present choice is $\overline{M} = 4$.

Similarly to what was described above for phase (I), $\hat{M} = 100$ off-grid parameter vectors are considered and for each of them pseudoexperimental results are generated and utilized to perform an identification by minimizing function ω of (12). It is worth noting that such minimization is to be performed not in the six-dimensional parameter domain over which the grid is defined, but in its three-dimensional subdomain of the stress parameters.
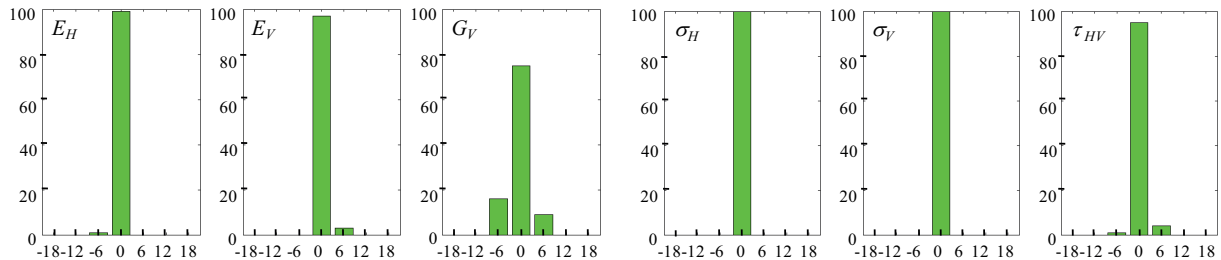
Figure 8. Performance of POD–RBF–TRA procedure for parameter identification based on pseudoexperimental DIC measurements affected by random noise of $\pm 5 \,\mu$m. In the abscissa, intervals of relative errors; in the ordinate, the percentage of errors found to fall within each such interval. Estimates of elastic moduli (first three diagrams) and stresses (remaining diagrams).

Figure 8b provides a visualization of the accuracy checks now concerning the POD–RBF–TRA estimation of the stresses σ_H σ_V τ_{HV} by means of $N = 2086$ measurements (over the ROI) of displacements, in transition from step (a) to step (b) (see Figure 2), after having introduced as preliminary data the estimates achieved for the elastic moduli by the preceding identification. The resulting mean error equals to: 0.65%, 0.96% and 1.51% for σ_H, σ_V and τ_{HV}, respectively.

The conclusion of the computations described (and other omitted for brevity) is rather encouraging: the devised method centered on POD, RBF and TRA, confined to elastic behavior, turns out to provide parameter estimations of both elastic moduli and pre-existing stresses which are expected to be fairly satisfactory in practical applications.

4. Identification of elastic moduli and stresses by a POD–ANN procedure

4.1. *The inverse analysis procedure.* Soft-computing methods, particularly artificial neural networks (ANN), are more and more frequently employed in engineering also to solve economically parameter identification problems (see e.g., [Waszczyszyn 1999; Fedele et al. 2005]). To the present purposes a conventional feed-forward neural network is adopted and optimized, in order to comparatively investigate an alternative to the POD–RBF–TRA procedure presented in what precedes. To achieve computational economies similar to those described in Section 3, POD is adopted again, and the compression of the information contained in the set of preliminary test simulations turns out to be useful for the reduction of the ANN input and for its useful "balance" with corresponding output.

The ANN is intended to provide the sought parameters p starting from the $\bar{M}$-dimensional amplitude vector $\bar{a}$ which corresponds to the N-dimensional experimental data vector u (snapshot) in the truncated basis $\bar{\boldsymbol{\Phi}}$ with $\bar{M} \ll M$, if M is the number of snapshots preliminarily computed by a FE code, like in the POD–RBF–TRA of Section 3. Since orthonormality is preserved in $\bar{\boldsymbol{\Phi}}$ after truncation, (7) gives rise to the relationship

$$\bar{A} = \bar{\boldsymbol{\Phi}}^T U. \tag{23}$$

This equation can be specialized to the link between any snapshot u_h (corresponding, through experiment or its simulation, to a parameter vector p_h) and its compacted amplitude $\bar{a}_h$, namely

$$\bar{a}_h\,(p_h) = \bar{\boldsymbol{\Phi}}^T u_h\,(p_h) \qquad \text{where} \quad h = 1, \ldots, M. \tag{24}$$

The $N \times \bar{M}$ matrix $\bar{\boldsymbol{\Phi}}$ (where N is the number of experimental or pseudoexperimental data and $\bar{M}$ the number of preserved eigenvalues of the matrix $D = U^T U$) is computed once and for all by the same POD procedure presented in Section 3. Equation (24) is essential for the generation of an ANN able to routinely estimate, fast and possibly in situ, the parameters p on the basis of input $\bar{a}$ representative of measurements u through (24) again.

The kind of ANN adopted here is a traditional one and can be outlined as follows (details in [Bishop 1995; Hagan et al. 1996; Bishop 2006])

The chosen ANN category is usually called *feed-forward multilayer perceptron.* Its architecture consists of a sequence of neurons layers (input, hidden, output). The transformation performed by each neuron in each active layers (not in the input layer) on received signals consists of a linear combination (by coefficients to be calibrated, called *weights* and *biases*, all gathered in a vector w) and a sigmoid

transform. The vector $\boldsymbol{w}$ is computed by minimizing a function Ω that quantifies the discrepancy between expected parameters $\boldsymbol{p}_h$ (targets) related to the amplitude $\bar{\boldsymbol{a}}_h$ through (24), and their counterparts generated by the ANN to be trained and, hence, related to the vector $\boldsymbol{w}$ of the minimization variables. Namely, the problem to solve for the ANN calibration is

$$\min_{\boldsymbol{w}} \Omega(\boldsymbol{w}) = \min_{\boldsymbol{w}} \left\{ \sum_{h=1}^{M} \left\| \boldsymbol{p}_h(\bar{\boldsymbol{a}}_h) - \boldsymbol{p}'_h(\boldsymbol{w}, \bar{\boldsymbol{a}}_h) \right\| \right\}. \tag{25}$$

The preselected parameter nodes $\boldsymbol{p}$ in the grid over the domain chosen in the $\boldsymbol{p}$-space, and the corresponding, preliminarily computed, snapshots $\boldsymbol{u}$ together with the associated amplitudes $\bar{\boldsymbol{a}}$ after POD, provide, without additional computations, a set of M *patterns* (pairs of $\bar{\boldsymbol{a}}_h$ and corresponding targets $\boldsymbol{p}_h$). These patterns are employed partly for ANN training as above (see (25)), and also partly for testing and validating the ANN. These computational processes are carried out once-and-for-all in order to optimize the architecture of the ANN for routine later use. ANN optimization is here intended, as usual, to avoid overfitting and roughness in the parameter estimations.

The solution $\boldsymbol{w}^*$ of problem (25) is achieved by the popular Levenberg–Marquardt algorithm, i.e., by first order mathematical programming in its back-propagation version, often employed for training feed-forward ANNs; see [Haykin 1998; Waszczyszyn 1999; Bishop 2006], for example.

4.2. *Validation by numerical examples.*

The chosen domain in the parameter space and grid are again those specified in Table 1. Therefore the $N \times M$ matrices $\boldsymbol{U}$ containing DIC pseudoexperimental data preliminarily computed once-and-for-all by FE simulations (Figure 4) have dimensions $N = 2086$, $M = 1089$ and $N = 2086$, $M = 3375$ for the identification of elastic moduli and of stresses, respectively.

Also the two POD procedures are the same as in Section 3 but now they are intended to compress the information contained in the snapshots in order to provide amplitudes in a new truncated basis $\bar{\boldsymbol{\Phi}}$ as input for a suitably trained ANN. The set of snapshots is subdivided into three subsets for various roles in ANN calibration: 70% for training; 15% for testing; 15% for validation. All pseudoexperimental data in $\boldsymbol{U}$ are modified by random errors in the range $\pm 5 \, \mu$m.

The number of amplitude components and the number of neurons in the ANN hidden layer (after a priori choice of an ANN with a single hidden layer architecture) are here established by the following optimization procedure: the mean error is assessed as a function of the neuron number in the hidden layer H and in the input layer I. The latter neuron number coincides with the dimensionality $\bar{M}$ of the amplitude vector generated by the truncated POD.

Figure 9 shows the influence of H with $I = 3$ and $I = 6$ on the ANN devoted to estimation of elastic parameters. The mean errors in Figure 9 are the averages in percentage of the differences between the expected exact parameters (called *targets*) and their values resulting from ANN training and testing. As a conclusion, the process of generating and checking the computational tool POD-ANN for later routine estimation of the three elastic parameters, leads to the choice of $I = 3$ neurons in input layer and $H = 6$ in hidden layer.

As for the identification of stresses σ_{H}, σ_{V} and τ_{HV} by means of the DIC measurements in phase (b) of the flat-jack test (Figure 2), the input layer of the second ANN must include three additional neurons to receive the estimates of elastic parameters based on DIC data from phase (c), besides the neurons that receive the amplitude $\bar{M}$-vector generated by the truncated POD, (23)+(24), of the snapshot $\boldsymbol{u}$ provided
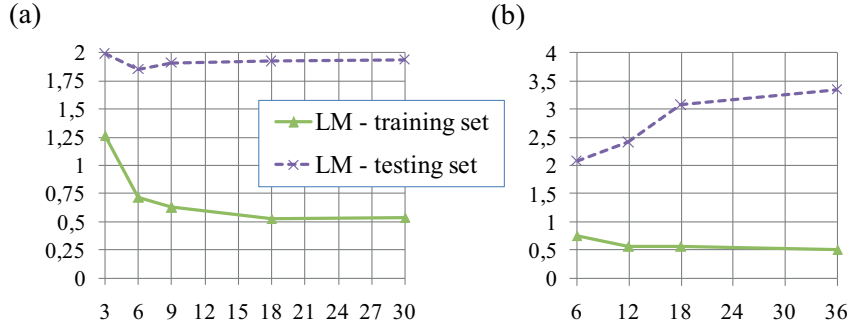
Figure 9. Influence of H, the number of neurons in the hidden layer, on the POD-ANN procedure for estimating the elastic parameters for (a) three and (b) six neurons in the input layer.
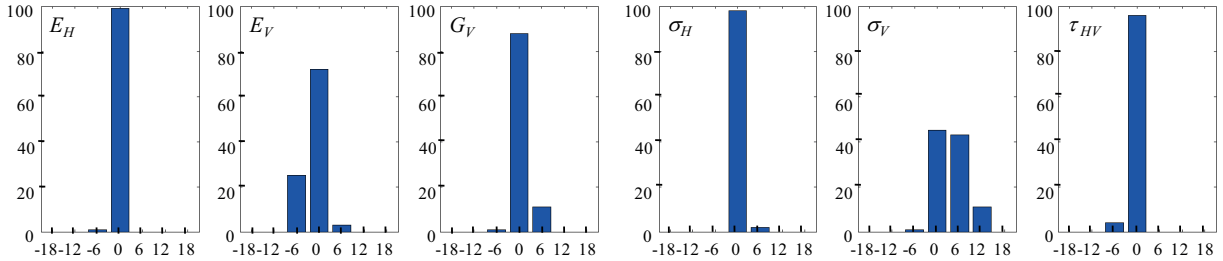
Figure 10. Performance of POD–ANN procedure for parameter identification based on pseudoexperimental DIC measurements affected by random noise of $\pm 5.0\,\mu$m. In the abscissa, intervals of relative errors; in the ordinate, the percentage of errors found to fall within each such interval. Estimates of elastic moduli (first three diagrams) and stresses (remaining diagrams).

by DIC. Now $M = 3375$, consistently with Table 1, and, hence, matrix U has dimensions $N \times M = 2086 \times 3375$. The design of the ANN for stresses, through considerations similar to those outlined above for elastic properties (again with random noise $\pm 5\,\mu$m) here omitted for brevity, leads to the following ANN architecture: 7–14–3. The set of 100 samples employed for the final accuracy checks of the POD–RBF–TRA inverse analysis procedure developed in Section 3, has been used for similar checks on the alternative procedure POD–ANN described in the present section. Results concerning elastic moduli and stresses are presented in Figure 10. A comparison of these results with those achieved in Section 3 and illustrated in Figure 8 leads to the conclusion that both procedures POD–RBF–TRA and POD–ANN associated with flat-jack test with T-geometry and to DIC full-field measurements are adequate to the identification of orthotropic elasticity parameters and pre-existing plane-stress state. Computer efforts and estimation accuracy are comparable.

5. Estimation of inelastic parameters

Inelastic parameters, not estimated by flat-jack tests in the state-of-the-art diagnostic methodology, are the objectives of the operative steps (d) and (e) and of the identification phase (III) in the present method

(Section 2.2 and Figure 2). A simplification which is adopted herein for inelastic parameter identification consists of the following two assumptions: (i) elastic isotropy, consistently with the isotropy attributed to the inelastic model; (ii) a pre-existing plane stress state in which σ_H is the only nonvanishing stress component. The elastic modulus E and the stress σ_H are supposed to have been identified in the previous phases of the procedure.

The concrete inelastic parameters to identify are internal friction angle β, tensile strength f_t and fracture energy G_f; the dilatancy $\psi = 40°$ is regarded as assumed a priori.

The experimental data supposed to be provided by a DIC photo, now over the smaller area (ROI) shown in Figure 2d-e, consist of $N = 210 \times 2 = 420$ displacement components on the dam surface. The reduction of the ROI implies a higher resolution in measuring the displacements due to inelastic strains and quasi-brittle fracture which occur when pressure is increased beyond the elastic threshold. Here it is assumed that the flat-jack pressure is increased up to the value of $10\,\mathrm{MPa}$ and that a sequence of 6 photos is taken at pressure levels $p = 5, \ldots, 10\,\mathrm{MPa}$ (with increments of $1\,\mathrm{MPa}$).

The inverse problem, (12), is now reformulated so that the displacements monitored at distinct load levels be all involved in the definition of the residual R and, hence, of the discrepancy function to minimize. To this purpose vector u becomes a vector consisting of 6 subvectors, each one representing the displacements of the ROI grid-nodes at one of the considered pressure levels. Therefore, henceforth in this section, the term snapshot will denote a vector u with $6N = 2520$ components. It is worth noting that the response of the system, now nonlinear under the applied pressure, is influenced by the effects (mainly the self-stresses) generated during the slot cutting, i.e during the operative step (b) of the experimental procedure (see Section 2.2). Such effects are accounted for in the FE simulations of the whole experimental procedure.

The FE model is substantially the same as the one employed for the preceding simulations, Figure 4a and Figure 4b; only a local mesh refinement is carried out over a volume in the vicinity of the free surface where the ROI is located, in order to accurately compute displacements at the ROI grid-nodes.

The expert-preselected domain for the three parameters sought is defined as follows:

$$1 \leq f_t \leq 6\,\mathrm{MPa}, \qquad 50 \leq G_f \leq 300\,\mathrm{Nm^{-1}}, \qquad 40° \leq \beta \leq 80°. \qquad (26)$$

In view of the novelty of flat-jack diagnostic tests and of inverse analyses based on them beyond the elastic range, the identifiability of the three parameters β, f_t and G_f has been investigated by various numerical exercises, some of which are outlined in what follows.

(A) Using the trust region algorithm (TRA) outlined in Section 3 (but here without POD preliminaries), parameter identifications are carried out using the following reference values of the constitutive parameters and the stress σ_H:

$$\text{elastic parameters and stress:} \quad E_H = 15\mathrm{GPa} \quad \nu = 0.2 \quad \sigma_H = -3\,\mathrm{MPa}$$
$$\text{inelastic parameters:} \quad f_t = 3\,\mathrm{MPa} \quad \beta = 68° \quad G_f = 180\,\mathrm{N/m}$$

The input consists of all 2520 pseudoexperimental DIC data generated by a simulation with the FE model of Figure 4, with the material model of Section 2; first inverse analysis is performed and illustrated in Figure 11a, starting from input data perturbed by a random noise governed by uniform probability density

(a)   (b)
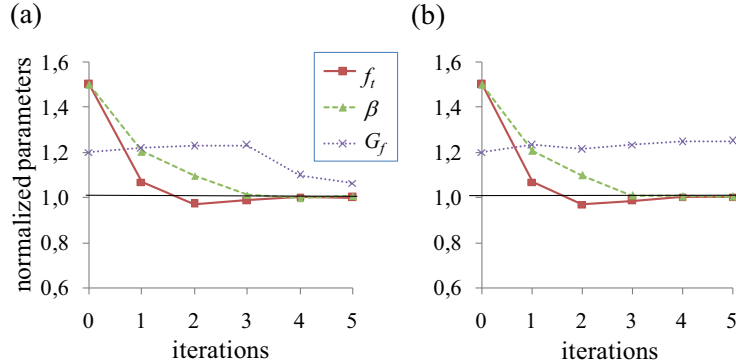
Figure 11. Convergence of TRA applied to inelastic parameter identification with input perturbed by random noise of (a) $\pm 0.25\,\mu$m and (b) $\pm 0.5\,\mu$m.

function over the interval $\pm 0.25\,\mu$m. With the same initialization and similar input perturbation amplified to $\pm 0.5\,\mu$m the TRA consequence is shown in Figure 11b.

This computational exercise (and others not considered here) shows stability of the estimation procedure with respect to (expected) experimental inaccuracies.

(B) In order to endorse the identification of inelastic parameters with the advantages of POD exhibited by the methodology presented in the preceding sections, the extended POD–ANN procedure (Section 4) is presented here below by means of a numerical exercise.

Clearly, in the present context, the ANN to design must be fed not only with the amplitude $\bar{a}$ (in the truncated basis $\overline{\boldsymbol{\Phi}}$; see (6)) of the new experimental data vector $\boldsymbol{u}$, but also with the results of the preceding identifications of the elastic modulus E (isotropic case) and of the pre-existing stress σ_{H}. Therefore a five-dimensional parameter space has to be considered; by choosing in such space the preselected domain and grid specified in Table 2, the number of grid nodes and the of corresponding snapshots (to be computed by FE test simulations once-and-for-all) reach now 5346.

Only $\overline{M} = 6$ eigenvalues of the matrix $\boldsymbol{D} = \boldsymbol{U}^T\boldsymbol{U}$ of order $M = 5346$ are preserved in the POD compression (i.e., after POD truncation). Therefore, each snapshot vector $\boldsymbol{u}$ containing $N = 2520$ components is replaced by its amplitude $\bar{a}$ of 6 components only; the ANN input layer consists of $6 + 2 = 8$ neurons the additional two being grid values of E and σ_{H}.

The 5346 available patterns (node parameters $\boldsymbol{p}$ emerging from Table 2 and compressed amplitudes $\bar{a}$ of the corresponding snapshot $\boldsymbol{u}$) have been employed to train (using 3742 randomly selected patterns), test (using 802 patterns) and validate (using 802 patterns) an ANN of the kind specified in Section 4,

	E/GPa	$\sigma_{\mathrm{H}}/\text{MPa}$	f_t/MPa	$G_f/(\text{N/m})$	$\beta/^\circ$
min	10	-6	1	50	40
step	5	2	1	25	5
max	20	-2	6	300	80

Table 2. Grid in parameter space for phase (III) of the identification procedure.
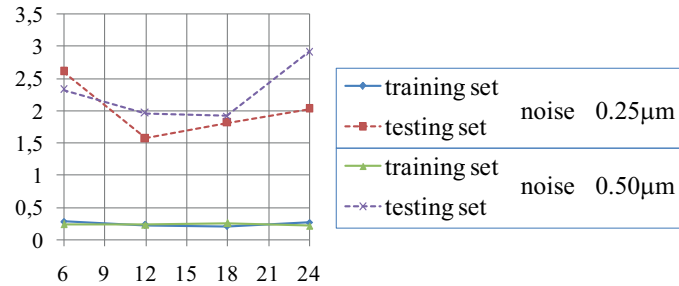
Figure 12. Influence of H, the number of neurons in the hidden layer, on the POD-ANN procedure for estimating the inelastic parameters for $I = 8$ input neurons.

by the same procedure outlined there. The optimal architecture turned out to consist of a single hidden layer with 12 neurons; see Figure 12.

The following numerical exercise (among others omitted for brevity) carried out by the POD–ANN procedure above, not only tests it but also provides motivation for further developments in terms of experimental techniques.

Over the five-dimensional domain specified by Table 2, a set of 100 points is randomly chosen. The corresponding snapshots are computed by the same FE and constitutive material models described in Section 2. Inverse analyses are performed, with perturbation noise of $\pm 0.25\,\mu$m and $\pm 0.50\,\mu$m, by POD–ANN calibrated in what precedes. The resulting estimates of inelastic parameters are compared to their "exact values" employed as input for the direct analyses which led to the snapshots. The differences are shown in Figure 13, in a fashion similar to that of Figures 8 and 10 for comparisons.

Clearly, the scatter of the estimation error for the fracture energy G_f is rather large. Such undesirable circumstance can be explained as follows: when preexisting horizontal compression σ_H or tensile strength f_t are rather large within the selected domain, with the assumed jack pressure the fracturing process is very limited and, therefore, fracture energy has small influence on the DIC measurable displacements; hence, larger becomes the sensitivity of its estimate to perturbations (including experimental errors and round-off errors in the numerical identification procedure).
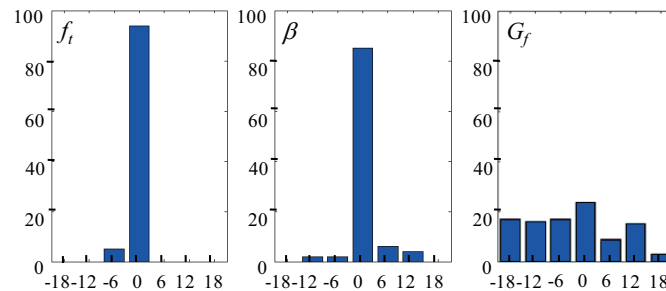
Figure 13. Performance of POD–ANN procedure for inelastic parameter identification based on pseudoexperimental DIC measurements affected by random noise of $\pm 0.5\,\mu$m. In the abscissa, intervals of relative errors; in the ordinate, the percentage of errors found to fall within each such interval.

Possible remedies, consistent with desirable progress in dam monitoring practice, are the following provisions: (i) an assessment of the crack opening displacement near the slot tip is extracted from the DIC measurements and employed to control the pressure growth in the flat-jack; the test is performed when the assessed displacement exceeds a pre-established threshold; (ii) two additional vertical slots are cut as shown in Figure 2f in order to practically eliminate the horizontal compressive stress.

Provision (i) would imply that the jack pressure is no longer selected a priori, once and for all, but becomes variable and represents an additional input into the ANN. The geometry change (ii) obviously makes the test somewhat more costly and more destructive. Both of these prospects could be worth of further investigations.

6. Closing remarks

The procedure resulting from this study on diagnostic analysis of concrete dams based on flat-jack tests, exhibits the following main advantages with respect to the present practice and also with respect to recent results achieved on the same subject (see e.g., [Fedele and Maier 2007]): (a) less damaging slots, due to the T-shaped geometry adopted here; (b) more experimental data which can be economically acquired by digital image correlation (DIC) and which regularize the inverse problem to solve; (c) assessment of inelastic properties of concrete, besides the elastic ones and the stress state considered so far; (d) computational efforts concentrated in a preparatory stage of multiple test simulations (say by a finite element commercial code) and much alleviated in applications, which can now be performed routinely in situ, either by soft computing, specifically by means of artificial neural networks (ANN), or by a popular mathematical programming procedure (TRA).

Besides obvious improvements of FE modeling and of constitutive models, meaningful further developments (which are partly in progress and partly desirable in the near future) can be listed as follows: (i) experimental validation in real-life engineering circumstances, particularly, as for the operative aspects of DIC measurements, on a concrete dam surface, after selection of suitable instruments and supports; (ii) improved jacks, with suitable textile instead of steel sheet in order to reduce friction and weld effects, and with larger radius complying with possible large size of aggregate in dam concrete; (iii) extension of the present approach and methodology to inhomogeneous periodic materials such as masonry, on which traditional flat-jack tests are frequently adopted to structural diagnosis purposes; (iv) transition from the present deterministic batch estimation methodology to the stochastic one (methodologically like, e.g., in [Fedele and Maier 2007] for a first step in this direction), with elaboration of both experimental data and their random errors in order to reach estimates accompanied by their covariance matrices.

An inverse analysis performable in situ with economy and brevity by exploiting preliminary computational results (and their POD approximation) achieved in a computing center, as proposed in this paper, turns out to be promising for structural diagnosis and for mechanical characterization, in dam engineering as well as in other technologies.

References

[Ahmed et al. 2003] T. Ahmed, E. Burley, S. Rigden, and A. Abu-Tair, "The effect of alkali reactivity on the mechanical properties of concrete", *Constr. Building Mater.* **17**:2 (2003), 123–144.

[Ardito et al. 2008] R. Ardito, G. Maier, and G. Massalongo, "Diagnostic analysis of concrete dams based on seasonal hydrostatic loading", *Eng. Struct.* **30**:11 (2008), 3176–3185.

[Avril et al. 2008] S. Avril, M. Bonnet, A. Bretelle, M. Grediac, F. Hild, P. Ienny, F. Latourte, D. Lemosse, S. Pagano, E. Pagnacco, et al., "Overview of identification methods of mechanical parameters based on full-field measurements", *Exp. Mech.* **48**:4 (2008), 381–402.

[Bishop 1995] C. M. Bishop, *Neural networks for pattern recognition*, The Clarendon Press Oxford University Press, New York, 1995. With a foreword by Geoffrey Hinton.

[Bishop 2006] C. M. Bishop, *Pattern recognition and machine learning*, Springer, New York, 2006.

[Buhmann 2003] M. D. Buhmann, *Radial basis functions: theory and implementations*, vol. 12, Cambridge Monographs on Applied and Computational Mathematics, Cambridge University Press, Cambridge, 2003.

[Chatterjee 2000] A. Chatterjee, "An introduction to the proper orthogonal decomposition", *Current Sci.* **78**:7 (2000), 808–817.

[Coleman and Li 1996] T. F. Coleman and Y. Li, "An interior trust region approach for nonlinear minimization subject to bounds", *SIAM J. Optim.* **6**:2 (1996), 418–445.

[Comi et al. 2009] C. Comi, R. Fedele, and U. Perego, "A chemo-thermo-damage model for the analysis of concrete dams affected by alkali-silica reaction", *Mech. Mater.* **41**:3 (2009), 210–230.

[Conn et al. 2000] A. R. Conn, N. I. M. Gould, and P. L. Toint, *Trust-region methods*, MPS/SIAM Series on Optimization, Society for Industrial and Applied Mathematics (SIAM), Philadelphia, PA, 2000.

[Fedele and Maier 2007] R. Fedele and G. Maier, "Flat-jack tests and inverse analysis for the identification of stress states and elastic properties in concrete dams", *Meccanica* **42**:4 (2007), 387–402.

[Fedele et al. 2005] R. Fedele, G. Maier, and B. Miller, "Identification of elastic stiffness and local stresses in concrete dams by in situ tests and neural networks", *Struct. Infrastruct. Eng.* **1**:3 (2005), 165–180.

[Fedele et al. 2006] R. Fedele, G. Maier, and B. Miller, "Health assessment of concrete dams by overall inverse analyses and neural networks", *Int. J. Fract.* **137**:1-4 (2006), 151–172.

[Goodman 1989] R. E. Goodman, *Introduction to rock mechanics*, 2nd ed., Wiley, New York, 1989.

[Hagan et al. 1996] M. T. Hagan, H. B. Demuth, and M. H. Beale, *Neural network design*, PWS Publishing, Boston, 1996.

[Hassing et al. 2010] P. M. Hassing, H. Fang, and Q. Wang, "Identification of material parameters for McGinty's model using adaptive RBFs and optimization", *Struct. Multidiscip. O.* **42**:2 (2010), 233–242.

[Haykin 1998] S. Haykin, *Neural networks: a comprehensive foundation*, 2nd ed., Prentice Hall, Upper Saddle River, NJ, 1998.

[Hild and Roux 2006] F. Hild and S. Roux, "Digital image correlation: from displacement measurement to identification of elastic properties: a review", *Strain* **42**:2 (2006), 69–80.

[Jirasek and Bazant 2001] M. Jirasek and Z. P. Bazant, *Inelastic analysis of structures*, Wiley, New York, 2001.

[Kleiber et al. 1997] M. Kleiber, H. Antunez, T. D. Hien, and P. Kowalczyk, *Parameter sensitivity in nonlinear mechanics: theory and finite element computations*, John Wiley, Chichester,NY, 1997.

[Leite and Corthesy 2001] M. H. Leite and R. Corthesy, "Stress measurements in concrete structures with modified doorstopper technique", *ACI Struct. J.* **98**:5 (2001), 619–628.

[Liang et al. 2002] Y. C. Liang, H. P. Lee, S. P. Lim, W. Z. Lin, K. H. Lee, and C. G. Wu, "Proper orthogonal decomposition and its applications. I. Theory", *J. Sound Vibration* **252**:3 (2002), 527–544.

[Loh and Wu 2000] C. H. Loh and T. C. Wu, "System identification of Fei-Tsui arch dam from forced vibration and seismic response data", *J. Earthquake Eng.* **4**:4 (2000), 511–537.

[Lubliner 1990] J. Lubliner, *Plasticity theory*, MacMillan, New York, 1990.

[Maier et al. 2004] G. Maier, R. Ardito, and R. Fedele, "Inverse analysis problems in structural engineering of concrete dams", pp. 97–107 in *Computational mechanics*, edited by Z. H. Yao et al., Tsinghua Univ. Press, Beijing, 2004.

[Nabney 2002] I. Nabney, *NETLAB: algorithms for pattern recognition*, Springer, London, 2002.

[Nocedal and Wright 1999] J. Nocedal and S. J. Wright, *Numerical optimization*, Springer Series in Operations Research, Springer-Verlag, New York, 1999.

[Ostrowski et al. 2008] Z. Ostrowski, R. Bialecki, and A. Kassab, "Solving inverse heat conduction problems using trained POD-RBF network inverse method", *Inverse Prob. Sci. Eng.* **16**:1 (2008), 39–54.

[Swamy 1992] R. N. Swamy, *The alkali-silica reaction in concrete*, Van Nostrand Reinhold, New York, 1992.

[Waszczyszyn 1999] Z. Waszczyszyn, *Neural networks in the analysis and design of structures*, Springer, New York, 1999.

[Wu 1995] Z. M. Wu, "Compactly supported positive definite radial functions", *Adv. Comput. Math.* **4**:3 (1995), 283–292.

[Wu et al. 2003] C. G. Wu, Y. C. Liang, W. Z. Lin, H. P. Lee, and S. P. Lim, "A note on equivalence of proper orthogonal decomposition methods", *J. Sound Vibration* **265**:5 (2003), 1103–1110.

TOMASZ GARBOWSKI: tomasz.garbowski@put.poznan.pl
Poznan University of Technology, Institute of Structural Engineering, ul. Piotrowo 5, 60-965 Poznan, Poland

GIULIO MAIER: giulio.maier@polimi.it
Dipartimento di Ingegneria Strutturale, Politecnico di Milano, Piazza Leonardo da Vinci 32, I-20133 Milan, Italy
giulio.maier@polimi.it

GIORGIO NOVATI: giorgio.novati@polimi.it
Dipartimento di Ingegneria Strutturale, Politecnico di Milano, Piazza Leonardo da Vinci 32, I-20133 Milan, Italy